

Carotid vasculature modeling from patient CT angiography studies for interventional procedures simulation

M. Freiman · L. Joskowicz · N. Broide · M. Natanzon ·
E. Nammer · O. Shilon · L. Weizman · J. Sosna

Received: 2 November 2011 / Accepted: 11 February 2012
© CARS 2012

Abstract *Objective* A practical method for patient-specific modeling of the aortic arch and the entire carotid vasculature from computed tomography angiography (CTA) scans for morphologic analysis and for interventional procedure simulation.

Materials and methods The method starts with the automatic watershed-based segmentation of the aorta and the construction of an a-priori intensity probability distribution function for arteries. The carotid arteries are then segmented with a graph min-cut method based on a new edge weighting function that adaptively couples voxel intensity, intensity prior, and local vesselness shape prior. Finally, the same graph-cut optimization framework is used to interactively remove a few unwanted veins segments and to fill in minor vessel discontinuities caused by intensity variations.

Results We validate our modeling method with two experimental studies on 71 multicenter clinical CTA datasets, including carotid bifurcation lumen segmentation on 56 CTAs from the MICCAI'2009 3D Segmentation Challenge. Segmentation results show that our method is comparable to the best existing methods and was successful in modeling the entire carotid vasculature with a Dice similarity measure of 84.5% (SD = 3.3%) and MSSD 0.48 mm (SD = 0.12 mm.) Simulation study shows that patient-specific simulations with

four patient-specific models generated by our segmentation method on the ANGIO Mentor™ simulator platform are robust, realistic, and greatly improve the simulation.

Conclusion This constitutes a proof-of-concept that patient-specific CTA-based modeling and simulation of carotid interventional procedures are practical in a clinical environment.

Keywords Carotid arteries · CTA · Segmentation · Model-based graph-cut

Introduction

Minimally invasive endovascular surgeries, involving the carotid vasculature, coronary arteries, and the heart are performed frequently. Even when performed by physicians with broad experience and expertise, they involve time-consuming trial and error with repeated contrast agent injection and angiography, leading to significant X-ray exposure for patients and health care professionals and to subsequent complications rates that are not negligible [1–3]. Training simulators such the ANGIO Mentor™ [4] have the potential to significantly reduce physicians learning curves, improve their performance, reduce exposure to ionizing radiation, and improve outcomes. Academic prototypes and commercial products provide hardware for haptic feedback and software enabling realistic simulations for a variety of interventional angiographic procedures, including catheterization and stenting [2,5–7]. To date, simulator libraries include only a limited, hand-crafted repertoire of models developed from patient scans or anatomical atlases. This limits their usefulness to skills training and learning assessment for residents and junior physicians.

Recent studies show that preoperative patient-specific simulation of complex endovascular procedures has a strong

M. Freiman (✉) · L. Joskowicz · N. Broide · M. Natanzon ·
L. Weizman
School of Engineering and Computer Science,
The Hebrew University of Jerusalem, Jerusalem, Israel
e-mail: freiman@cs.huji.ac.il

E. Nammer · O. Shilon
Symbionix Ltd., Lod, Israel

J. Sosna
Department of Radiology, Hadassah-Hebrew University
Medical Center, Jerusalem, Israel

influence on tool selection, angiographic imaging, and contrast agent injection for expert physicians [8–13]. The studies also show that preoperative rehearsal has the potential to reduce the radiation dose, to reduce the number of endovascular devices that are used, and to reduce complications, by allowing physicians to gain valuable insights into patient anatomy before the intervention.

Routine usage of presurgical patient-specific simulation requires automatic, fast, and accurate vasculature modeling from computed tomography angiography (CTA) images. Currently, a laborious process by a computer modeling expert is required to generate patient-specific models with the detail, accuracy, and quality required for simulation. For example, [8] reports a user interaction time of 60–100 min to generate patient-specific vascular models for simulation. Patient-specific model generation is the major bottleneck preventing introduction of these rehearsal systems into routine clinical practice [8].

Endovascular patient-specific simulation requires the accurate segmentation of the entire lumen of the vascular anatomy. For example, the relevant anatomy for carotid bifurcation stent implantation includes the common carotid artery (CCA), extracranial internal carotid artery (ICA), external carotid artery (ECA) and its branches, the carotid bifurcation (CB), subclavian arteries (SA), and aortic arch (AA). The vertebral arteries are helpful but not required for simulation. These vascular structures are characterized by wide intra- and inter-patient intensity and architecture variations, and are proximal to bone structures with similar intensity values. Imaging artifacts caused by metallic objects such as dental implants are common. In addition, in many patients, severe stenosis around the carotid bifurcation may cause segmentation failure [14]. Common modeling flaws include inaccurate vessel diameters, missing vessel segments and entire small vessels, inclusion of nonvascular anatomical structures, and incorrect modeling of bifurcations and pathology.

In this paper, we present a complete framework for preoperative CTA scan-based patient-specific carotid artery modeling. Our method enables the generation of patient-specific simulations in a clinically acceptable time frame without the need of dedicated technician. It includes a model-based graph-cut segmentation method that couples a patient-specific vessel intensity model and local vesselness shape priors in a graph-based segmentation approach. To correct the inevitable inaccuracies, we have developed a semi-automatic graph-based editing tool to remove unneeded veins and fill in minor discontinuities around the bifurcation of the common carotid from the aortic arch caused by contrast agent injection artifacts.

The main contributions of this paper are: (1) a model-based graph-cut approach to vessel segmentation based on an automatically generated patient-specific vessel intensity model and local vesselness tubular shape priors; (2) a new

patient-specific carotid vasculature modeling framework for preoperative simulation; and (3) an extensive, multicenter, multiobserver evaluation using clinical CTA datasets. To the best of our knowledge, ours is the first work that addresses the segmentation of the entire carotid vasculature that is required for carotid bifurcation stent implantation simulation from CTA images. Our study includes both a quantitative and a qualitative evaluation of segmentation accuracy and the simulation process on a publicly available database. Thus, our work provides a proof-of-concept of clinically practical patient-specific carotid vascular system modeling for preoperative patient-specific interventional endovascular procedure simulations.

The rest of this paper is organized as follows. In “Previous work,” we review the state of the art in carotid artery segmentation. In “Method,” we describe our methods in detail. In “Experimental results,” we describe three experimental studies that validate the proposed approach. “Conclusion” concludes the paper with a discussion and description of future work.

Previous work

Carotid artery segmentation from CTA scans is a challenging task. The main difficulties are significant intra- and inter-patient carotid intensity and geometry variability [15], intensity value overlap of carotid arteries and neck vertebrae, and dental implant streaking artifacts. Numerous automatic and semi-automatic segmentation methods for various anatomical structures and imaging modalities have been developed during the past decade. For a general review of these methods see [16, 17].

The main approaches for carotid artery segmentation rely on intensity values [18], geometrical shape information [19, 20], edge-based active contours [21–25], statistical active shape models [26], and contour tracking [14, 27–29]. Some of these methods were developed for magnetic resonance angiography (MRA) and for digital subtraction angiography (DSA) scans [18–22, 24]. They produce good results on specific vascular regions of radiological interest in which vessel intensity is clearly distinct from the intensity of nearby organs. However, these methods were not validated for the segmentation of the entire extra-cranial carotid system.

Hybrid approaches, such as [30] use an automatic partitioning formulation that selects a different segmentation algorithm for each part of the carotid vasculature. This partition algorithm was validated; however, no quantitative analysis of segmentation accuracy throughout the entire carotid vasculature and its fidelity for simulation was conducted.

The automatic active surface segmentation algorithm described in [31] requires accurate automatic registration to an atlas to identify the vascular system start and end points

for centerline computation. Its main drawbacks are that it is highly sensitive to precise identification of start and end points. The evaluation of this method on the publicly available CLS2009 database [32] shows that it failed to process 5 out of the 15 cases in the training datasets and 8 out of the 31 testing cases due to registration errors. The high dependency of this method on the success of the initial registration is undesirable in routine clinical usage.

A recently published technique [9] describes a method for the segmentation of the entire carotid system from CTA and MRA images for use in simulation. This method consists of (1) enhancement and cleaning the patient data with anisotropic diffusion and morphological operators; (2) segmentation of the vessels through a level set evolution, initialized from a manually selected threshold; (3) skeletonization to obtain the centerlines of the vessels; (4) estimation of the vessel surface through circle or ellipse fitting; and (5) cross section post-processing. The preprocessing step (i.e., 1) heavily depends on multiple parameters whose adjustment in wide clinical practice is undesirable. It is important to note that this method evaluated only on 2 CTA datasets that are not representing wide variety of patients and pathologies.

The graph min-cut segmentation method [33,34] classifies voxel nodes that separate objects of interest and background based on both weighted voxel adjacencies and prior intensity models of the object and the background. The advantages of graph min-cut segmentation are that it provides a globally optimal solution in polynomial time, that it is generic, and that it relies on a few parameters that do not require frequent adjustments. However, it has been recently reported that graph min-cut segmentation suffers from a “shrinking bias” [35,36]. It is thus less suitable for vasculature segmentation without user interaction or prior shape information [37].

Previous methods utilizing the graph min-cut segmentation method for vascular structures segmentation [29,38–41] were developed and tested for tasks other than segmentation of the entire carotid vasculature.

Recently, a Grand Challenge workshop devoted to the segmentation of a single carotid artery bifurcation was organized by the Medical Image Computing and Computer Aided Interventions (MICCAI) Society. (For details on the participating algorithms, datasets, evaluation methodology and results, see [42].) In our contribution to this workshop [43], we presented a semi-automatic tool for the segmentation of the carotid bifurcation.

However, the focus of the workshop was the segmentation of the carotid bifurcation. Therefore, the performance of the algorithms presented in the workshop, including ours, in segmenting the entire extracranial carotid vasculature remains unclear, especially because of intensity value overlap between these vessels and nearby organs [8,9]. It is the goal of this work to present a comprehensive method for the

segmentation and modeling of the entire carotid vasculature system for simulation.

Method

The input to our method is a routine clinical CTA scan of the head and the neck of the patient including the entire carotid vasculature from the aortic arch to the skull. Segmentation proceeds in four main steps (Fig. 1): (1) automatic aortic arch segmentation; (2) intensity and shape model generation; (3) automatic carotid, vertebral, and subclavian arteries segmentation; and (4) semi-automatic graph-based vessel connection and cleaning. The output is an accurate 3D geometric model of the carotids for morphological analysis and robust real-time simulation. We will now describe each of these steps in detail.

Aortic arch segmentation

Aortic arch segmentation relies on prior anatomical knowledge of the aortic arch structure, the aorta location, and its relative brightness. Our aortic arch segmentation algorithm starts with automatic identification of the region of interest (ROI) followed by watershed-based segmentation. We describe these steps in detail.

The aorta is the dominant arch-like vessel above the pulmonary artery located in the lower fourth region of a head and neck CTA scan acquired with an inferior to superior orienta-

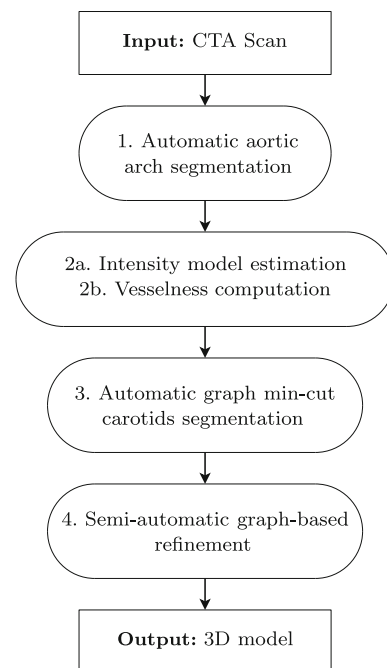


Fig. 1 Flowchart of the proposed segmentation method

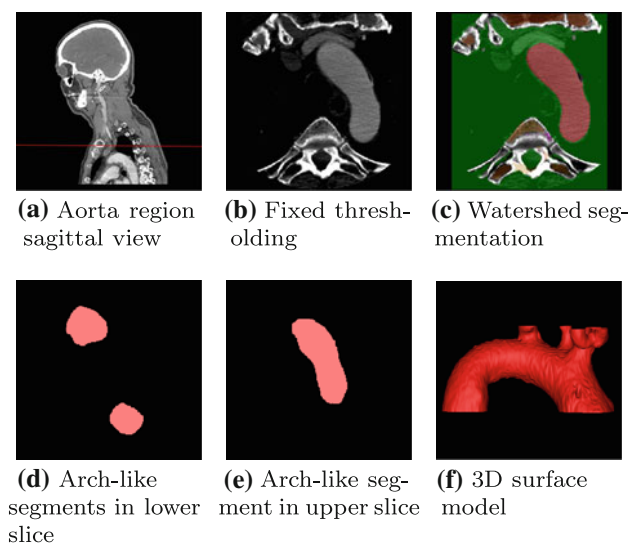


Fig. 2 Automatic aorta segmentation: **a** aortic arch region (sagittal view); **b** thresholded CTA scan axial slice; **c** watershed segmentation result; **d**, **e** arch-like structure as it appears in the lower (**d**) and upper (**e**) slices of the component; and **f** 3D surface model

tion. When the scan is acquired in a different patient position, we re-orient the scan to the inferior to superior orientation based on the position information stored in the DICOM format where available or by rigid registration.

First, the aorta ROI is defined as the lower quarter of the CTA scan (Fig. 2a). Background voxels, whose values are outside the expected vessel intensity range (0–600 Hounsfield Units) are eliminated (Fig. 2b). The watershed transform [44] is then applied to the gradient magnitude image to obtain an initial segmentation.

The resulting segmentation includes several connected components (Fig. 2c), with the aortic arch among them. To identify which one is the aortic arch, each component is examined individually as follows. For each CTA slice, the 2D segments that belong to each 3D component are identified by connected components analysis [45]. The aortic arch segments appear as two nearby circular segments in the lower slices (Fig. 2d), and as a single ellipsoid segment on the upper slices (Fig. 2e). A component is classified as arch-like when lower slices contain only two segments and the slices above contain only one segment. 2D segments with a small number of pixels (less than 800) in the upper slices correspond to vascular bifurcations from the aortic arch and are ignored. Finally, the intensity variance of each arch-like component is computed. The arch-like component with the lowest intensity variance corresponds to the aortic arch (Fig. 2f).

Intensity model estimation

Intensity probability distribution function (IPDF) of the vascular and nearby anatomical structures is automatically esti-

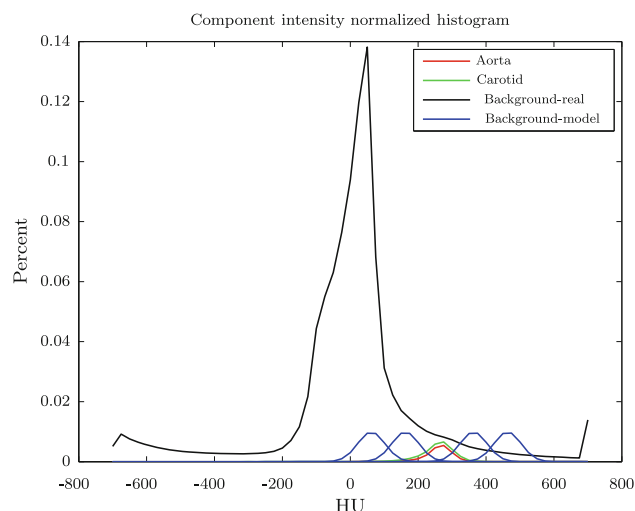


Fig. 3 Representative examples of the background (*black*), aorta (*red*), and carotids (*green*) histograms normalized by the overall number of voxels in the CTA scan and our implicit four-class background model (*blue*). Note that the carotid and the aorta histograms have very similar shapes, while the four-class background model covers the background intensities close to the carotid intensities. Note also that the intensity information alone is not sufficient to discriminate between the aorta, carotids, and the background

mated from the resulting aortic arch segmentation. Figure 3 shows representative normalized histogram of the aorta, carotid vasculature, and the rest of the CTA image. Both the aorta and carotid intensity values usually exhibit Gaussian distributions with similar parameters; thus, we use the aorta IPDF as an a priori intensity model for the carotid.

To model the background distribution, we observe that modeling it as the complement of the foreground will not represent accurately the presence of overlapping intensity values between the foreground and background classes. In addition, modeling background intensity values with a unimodal normal distribution [27], or with a bimodal distribution, in which one peak represents pixels darker than the carotid and the other represents pixels brighter than the carotid, will also yield a large variance in each background class, and thus may reduce the segmentation accuracy.

To overcome this problem, we model the background intensity implicitly with a four-class model [46] where each class is modeled as a normal distribution. The vascular system (object) class parameters are computed using the mean and the variance of the aortic arch. The background organs whose gray values are near/far and above/below the vascular system gray values are then modeled according to four background classes. The mean value of each class is computed with respect to the vascular system class mean value. Voxels with intensity values out of the four-class background model range are discarded.

Formally, the vascular system class X_{vs} is defined as:

$$X_{vs} \sim N\left(\mu_{vs}, \sigma_{vs}^2\right) \quad (1)$$

where μ_{vs} is the mean intensity value of the vascular system class and σ_{vs}^2 is its variance. The remaining four classes X_i are modeled as:

$$X_i \sim N(\mu_i, \sigma_i^2) \tag{2}$$

for each $i \in \{\text{near-low, near-high, far-low, far-high}\}$. The means of these classes are defined as:

$$\begin{aligned} \mu_{\text{near-high}} &= \mu_{vs} + (k_{\text{near}} \times \sigma_{vs}) \\ \mu_{\text{near-low}} &= \mu_{vs} - (k_{\text{near}} \times \sigma_{vs}) \\ \mu_{\text{far-high}} &= \mu_{vs} + (k_{\text{far}} \times \sigma_{vs}) \\ \mu_{\text{far-low}} &= \mu_{vs} - (k_{\text{far}} \times \sigma_{vs}) \end{aligned} \tag{3}$$

where the constants k_{near} and k_{far} values are determined once by comparing the segmentation results obtained with various parameter values on the training datasets to their ground truth segmentation obtained by expert manual segmentation, and choosing the best ones. In this model, each voxel from the ambiguous vascular system boundaries has a high probability of being in both the vascular system and in the ‘‘near’’ classes. Its final classification will be determined by the intensity values of its neighboring voxels.

Carotid arteries segmentation

The next task is to separate the carotid lumen (object) from the surrounding structures (background) in the CTA volume I . We define the carotid artery segmentation problem as a binary labeling problem in which a label $M(x) \in \{M_{\text{Obj}}, M_{\text{Bkg}}\}$ is assigned to each voxel x .

Following the Bayesian approach, the segmentation corresponds to the labeling map \hat{M} that maximizes the posterior probability of the Markov random field (MRF) associated with the label map:

$$\hat{M} = \underset{M}{\operatorname{argmax}} p(M|I) \propto p(I|M)p(M) \tag{4}$$

where:

$$\begin{aligned} p(I|M)p(M) &\propto \prod_x \phi(I(x)|M(x)) \prod_{y \in \Omega(x)} \psi(M(x), M(y)) \end{aligned} \tag{5}$$

and $\Omega(x)$ is the neighborhood around the voxel x .

This maximum a posterior MRF (MAP-MRF) inference problem is equivalent to the minimization of the energy functional [47]:

$$\begin{aligned} E(M) &= -\log(p(I|M)p(M)) \\ &= \sum_x \left(-\log(\phi(I(x)|M(x))) \right. \\ &\quad \left. + \sum_{y \in \Omega(x)} -\log(\psi(M(x), M(y))) \right) \end{aligned} \tag{6}$$

where $\phi(I(x)|M(x))$ is the likelihood of voxel x to have label $M(x)$ and $\psi(M(x), M(y))$ is the prior MRF smoothness term. Both $\phi(I(x)|M(x))$ and $\psi(M(x), M(y))$ are computed as follows [33]:

$$\begin{aligned} \phi(I(x)|M(x)) &= \exp\left(-\frac{(I(x) - \mu_{M(x)})^2}{2\sigma_{M(x)}^2}\right) \\ \psi(M(x), M(y)) &= \exp\left(-\frac{(I(x) - I(y))^2}{2\sigma_{M(x)}^2}\right) \end{aligned} \tag{7}$$

where $\mu_{M(x)}$ and $\sigma_{M(x)}$ are the mean and standard deviation of the class that assigned to voxel x .

As illustrated in Fig. 4a, b, the intensity model by itself is not sufficient to accurately differentiate between the carotid lumen and its surrounding tissue. Therefore, we use a hybrid model that integrates the intensity model with a local vesselness shape constraint. The new energy functional is defined as:

$$\begin{aligned} E(M) &= \sum_x \left(-\log(\phi^i(I(x)|M(x))) - \log(\phi^{vs}(\Theta(x)|M(x))) \right. \\ &\quad \left. + \sum_{y \in \Omega(x)} -\log(\psi'(M(x), M(y))) \right) \end{aligned} \tag{8}$$

where $\phi^i(I(x)|M(x))$ is the intensity-based term computed from the prior intensity model as follows:

$$\phi^i(I(x)|M(x)) = \begin{cases} p(I(x)|\mu_{vs}, \sigma_{vs}) & M_{\text{Obj}} \\ \max p(I(x)|\mu_i, \sigma_i) & M_{\text{Bkg}} \end{cases} \tag{9}$$

where $i \in \{\text{near-low, near-high, far-low, far-high}\}$, and $\Theta(x)$ is the local vesselness information computed with Frangi’s multiscale Hessian based vesselness filter [19]:

$$\mathcal{V}(\sigma) = \begin{cases} 0 & \lambda_2, \lambda_3 > 0 \\ \left(1 - e^{-\frac{R_A^2}{(2a)^2}}\right) \left(e^{-\frac{R_B^2}{(2b)^2}}\right) \left(1 - e^{-\frac{S^2}{(2c)^2}}\right) & \text{otherwise} \end{cases} \tag{10}$$

where

$$R_A = \frac{|\lambda_2|}{|\lambda_3|} \quad R_B = \frac{|\lambda_1|}{\sqrt{|\lambda_2\lambda_3|}} \quad S = \sqrt{\lambda_1^2 + \lambda_2^2 + \lambda_3^2} \tag{11}$$

and σ is the scale at which the measure is computed. The constant R_A is used to differentiate between plate and line-like structures. The constant R_B is used to measure the deviation from blob-like structures. The constant S is used to differentiate between vessels (foreground) and other structures (background). The constants a , b and c are predefined weights that determine the relative influence of R_A , R_B and S . The vesselness measure value is close to 1 for voxels with tube-like structures, and close to 0 otherwise, and is computed for each voxel and for each scale. Finally, for each voxel, the maximal value among the different scales is set to the voxel vesselness measure. The shape term $\phi^{vs}(\Theta(x)|M(x))$ is equal to $\Theta(x)$ for M_{Obj} and to $1 - \Theta(x)$ for M_{Bkg} .

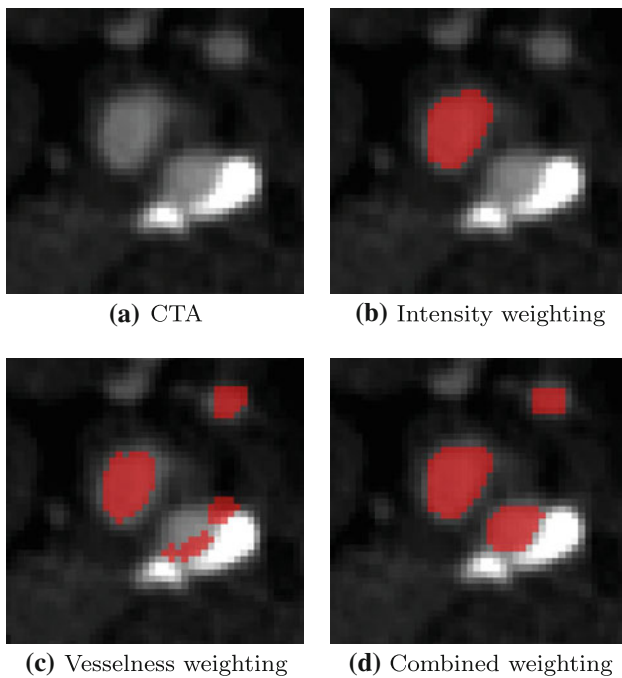


Fig. 4 Illustration of the need for a hybrid model for graph-cut segmentation (red): **a** original CTA slice of the carotid bifurcation; **b** intensity weighting; **c** vesselness weighting; **d** combined intensity and vesselness weighting

The penalty for two adjacent voxels x, y with different labels $\psi'(M(x), M(y))$ is based on their intensity difference and depends on the local shape information of the edge origin (x):

$$\begin{aligned} \psi'(M(x), M(y)) &= \exp\left(-\frac{(I(x) - I(y))^2}{2\sigma^2}\right) \cdot \left((1-\alpha) + \alpha \left(\frac{1}{\Theta(x) + \epsilon}\right)\right) \end{aligned} \quad (12)$$

Note that multiplication of the contrast and shape terms reduces the sensitivity to intensity differences in regions with high shape information and increases the sensitivity to intensity differences in regions with low vesselness response, which are more related to background. This cause our method to reduce the “shrinking bias” associated with the graph min-cut segmentation [35,36].

The weighting constant $\alpha \in [0, 1]$ controls the degree of smoothness with respect to the shape information; ϵ is a small constant to prevent dividing by zero.

This asymmetric formulation encourages the minimal cut solution to include voxels that are nearby voxels with high vesselness response (e.g., centerline voxels) inside the object class, ignoring minor intensity differences between them, while eliminating voxels with similar intensity values that are not near to voxels with high vesselness response, resulting in a segmentation boundary that coincides with the physical boundary of the vessel and.

Since $\psi'(\cdot, \cdot) \geq 0$, the energy functional in Eq. 8 satisfies the modularity condition:

$$\psi'(x, x) + \psi'(y, y) \leq \psi'(x, y) + \psi'(y, x) \quad (13)$$

where x, y are two adjacent voxels. Therefore, the globally optimal solution can be computed in polynomial time using the graph min-cut technique [47] as follows.

Let $G = (V, E)$ a directed graph, where $V = \{v_{x_1}, \dots, v_{x_n}, v_s, v_t\}$ are the graph nodes such that node v_x corresponds to voxel x and terminal nodes v_s and v_t correspond to the object and background classes. The graph edges $E = \{(v_x, v_s), (v_x, v_t), (v_x, v_y)\}$ consist of three groups:

1. edges (v_x, v_s) from voxels to the object terminal node;
2. edges (v_x, v_t) from voxels to the background terminal node, and;
3. directed edges (v_x, v_y) between adjacent voxels (6 or 26 neighbors for 3D images).

The cost of the cut C that divides the graph into the object class (source vertex) and the background class (terminal vertex) is defined as the sum of the weights of the cut edges $e \in C$.

Edge weights w_e are assigned as follows. Edge weights $w(v_x, v_s)$ represent the likelihood that voxel v_i is related to the vessels (object) class:

$$w(v_x, v_s) = -\log(\phi^i(I(x)|M_{Obj})) - \log(\phi^{vs}(\Theta(x)|M_{Obj})) \quad (14)$$

Edge weights $w(v_x, v_t)$ represent the likelihood that voxel x belongs to the background class:

$$w(v_x, v_t) = -\log(\phi^i(I(x)|M_{Bkg})) - \log(\phi^{vs}(\Theta(x)|M_{Bkg})) \quad (15)$$

where $\phi^i(I(x)|M_{Obj})$ and $\phi^i(I(x)|M_{Bkg})$ are the likelihoods that voxel x belongs to the object/background classes, based on the voxels intensity information and the background IPDF implicit model (Eqs. 2, 3), $\phi^{vs}(\Theta(x)|M_{Obj})$ is the local vesselness response (Eq. 10), and $\phi^{vs}(\Theta(x)|M_{Bkg})$ is the background shape information defined as $1 - \phi^{vs}(\Theta(x)|M_{Obj})$.

Edge weights $w(v_x, v_y)$ penalize for adjacent voxels that have different labels. The penalty depends on both the intensity contrast between the two voxels and the shape information.

$$w(v_x, v_y) = \psi'(M(x), M(y)) \quad (16)$$

where $\psi'(M(x), M(y))$ is defined in Eq. 12.

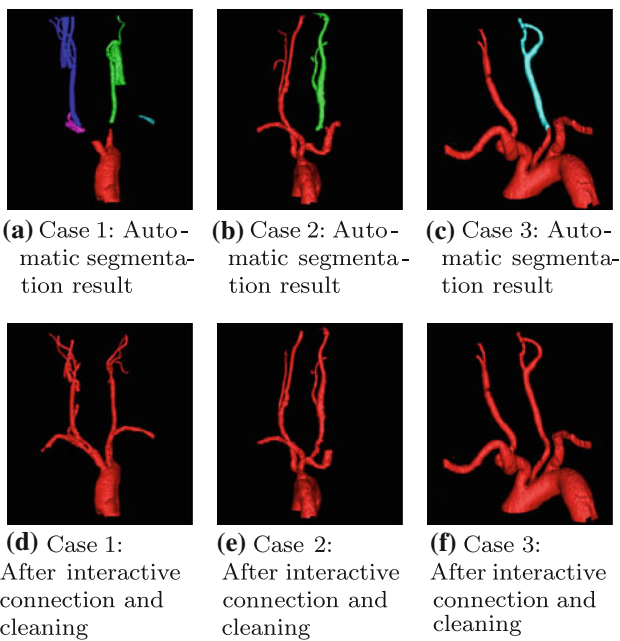


Fig. 5 3D visualizations of automatic vessel segmentation from 3 CTA studies. **a–c** Three representative vessel surface meshes constructed from automatic segmentation of CTA studies. *Blue* and *green* vessels are disconnected. **d–f** Vessel models after interactive connection and cleaning

Interactive semi-automatic graph-based vessels connection and cleaning

The automatic artery segmentation step may produce disconnected vessel segments, may miss small vessels, or may include the internal jugular veins. Figure 5a–c shows representative results on three examples. Note that the automatic method correctly segments the main parts of the carotid artery system, including the carotid bifurcation, the CCA, ICA, and ECA, with some of their secondary vasculature. In Fig. 5a, both connection of the CCA to the aortic arch and removal of the jugular veins are required. In Fig. 5b–c, connection of the right CCA to the entire carotid vasculature model is required.

We have developed an interactive, semi-automatic editing tool to allow the user to easily fix these flaws, remove unwanted blood vessels, and produce a 3D model of the entire carotid vasculature based on the automatic segmentation. Figure 5d–f shows the vasculature models after correction with the interactive tool.

The interactive tool requires the user to identify two points for each disconnected artery or undesired vein. It then computes the segmentation of the vessel in two steps: (1) vessel centerline estimation using a weighted shortest path algorithm; and (2) optimal vessel boundary segmentation using a spatially constrained graph min-cut. Once the vessel has been reconstructed, it is added to the vessels model generated by the previous automatic step, or removed from the automatic

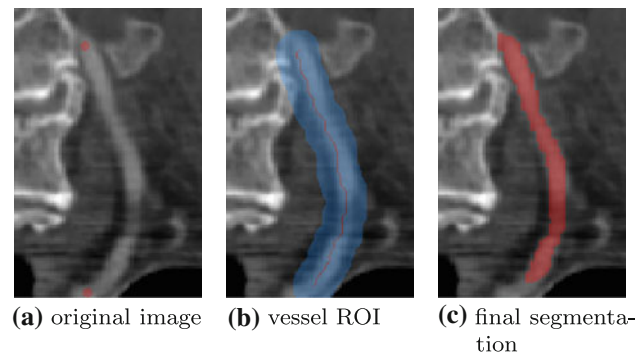


Fig. 6 Illustration of the segmentation process on a coronal CTA image depicting the left vertebral artery in a clinical study. Note strong imaging artifacts. **a** Original image with seed points; **b** weights map showing the shortest path (*red*) and the region of interest (*blue*); and **c** final segmentation

segmentation according to the user decision. Figure 6 illustrates the method. We will now describe each step in detail.

Vessel shortest path computation

The vessel shortest path is computed by finding the weighted shortest path between the graph nodes s and t corresponding to the user-defined vessel seed points. The shortest path is the sequence of edges connecting s to t for which the sum of edge weights is minimized. To achieve real-time performance, only intensity and image gradient information is used, as vesselness information [19] requires time-consuming eigen analysis of the second order derivatives.

The edge weighting function is defined as the weighted sum of (1) the local intensity difference; (2) the seed deviation intensity difference; (3) the image gradient smoothness along the path; and (4) the path length:

$$w(x, y) = a \cdot (I(x) - I(y))^2 + b \cdot \left((I(y) - I(s))^2 + (I(y) - I(t))^2 \right) + c \cdot |\cos^{-1}(\nabla I(x) \cdot \nabla I(y))| + k \quad (17)$$

The first term is the squared difference between voxel x , y intensity values. This term penalizes for intensity differences along the path and prevents the path from leaving the vessel region.

The second term is the sum of the relative squared differences of the seeds and edge-end voxel (y) intensity values. This term prevents the edges in the path from diverging from the intensity values of the user-defined seed points, and prevents the path from moving along locally smooth tissues with low edge weights instead of inside the noisy vessel.

The third term is the angle between the intensity gradients along the path. This term ensures the smoothness of the image gradients along the path. The constant k is used to penalize long paths.

The weighting constants a , b , c are used to normalize the terms and to control the effect of each term on the overall path weight. Their values were determined experimentally and set once for all datasets.

The shortest path is then computed using Dijkstra's algorithm [48].

Optimal vessel boundary segmentation

The vessel boundary segmentation is computed by spatially constrained graph min-cut optimization around the computed vessel path. A distance map that describes the path obtained in the previous step is used to spatially constrain the min-cut problem over the corresponding graph, as described in "Carotid arteries segmentation." Edge weights are assigned as follows.

Edge weights $w(x, s)$ penalize voxels whose intensity value is far from the mean intensity value along the computed vessel path:

$$w(x, s) = \exp\left(-\frac{(I(x) - \mu_p)^2}{2\sigma_p^2}\right) \cdot \frac{d(x)}{k} \quad (18)$$

where μ_p is the intensity mean value along the vessel path, σ_p is the intensity standard deviation along vessel path, $d(x)$ is the distance between the current voxel x and the vessel path, and k is a normalization factor. This weight represents our belief that voxel x belongs to the object class based on voxels intensity $I(x)$ and the objects mean intensity value combined with spatial information that favors voxels that are closer to the vessel path.

Edge weights $w(x, t)$ represent the likelihood that each voxel belongs to the background:

$$w(x, t) = 1 - w(x, s) \quad (19)$$

In this case, we use the complement of the object weight $w(x, s)$ instead of an explicit background intensity model ("Intensity model estimation"), because the ROI is small and consists primarily of desired vessel voxels, with fewer darker background voxels.

Edge weights $w(x, y)$ represent the magnitude of the local intensity difference between the adjacent voxels:

$$w(v_x, v_y) = \exp\left(-\frac{(I(x) - I(y))^2}{2\sigma_p^2}\right) \quad (20)$$

The minimal cut is computed as before, with Boykov's algorithm [33]. The solution represents the optimal surface that separates the image into the vessel object and the background. Figure 7 shows the segmentation results of three challenging examples after interactive correction.

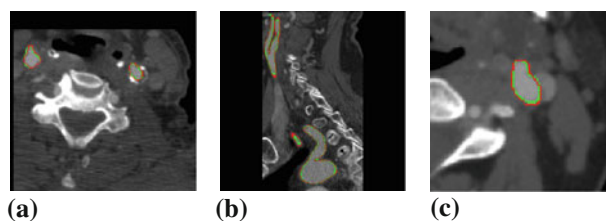


Fig. 7 Semi-automatic segmentation results: 2D views of segmentation results on representative datasets. The resulting segmentation contour (red) is overlaid on the ground truth contour (green). **a** Stenosis—axial view, **b** aortic arch and carotid bifurcation—sagittal view, **c** CCA—axial view

Experimental results

We validate our method with three experimental studies on multicenter clinical CTA datasets. The first study addresses the accuracy of the automatic and semi-automatic segmentation tool for the carotid bifurcation lumen on 56 CTAs from the MICCAI'2009 3D Segmentation Challenge for Clinical Applications Workshop (CLS2009) [42]. The second study addresses automatic segmentation followed by semi-automatic refinement of the entire carotid vascular system on a separate set of 15 CTAs from two medical centers, which were not included in the CLS2009 database. The third study addresses the simulation of interventional radiology procedures on patient-specific models generated by our segmentation method on the ANGIO MentorTM simulator platform. We describe parameter optimization and validation studies in detail below.

Parameter optimization

We have implemented our method in C++ using the ITK software library [49]. Segmentation parameters were optimized experimentally with three head and neck CTA scans acquired with acquisition parameters similar to those of the Hadassah-Hebrew University Medical Center datasets in the CLS2009 database [42]. For each dataset, the vascular system was segmented by a 3D segmentation expert and validated by an expert radiologist. The resulting parameter values were set once and for all in the following test datasets. The watershed transform parameters for the aortic arch segmentation *depth* and *lower-threshold* were optimized visually and set to *depth* = 0.25 and *lower-threshold* = 0.001.

The intensity model parameters k_{near} and k_{far} (Eq. 3) were set by observing the effect of their values on the overall segmentation accuracy on the three training datasets. The Dice measure was computed for the carotid bifurcation region in intervals $k_{\text{near}} \in [1.5, 3.5]$ and $k_{\text{far}} \in [4, 6]$ using equally spaced steps of 0.5. Figure 8 summarizes segmentation results with varying parameter values. Based on these

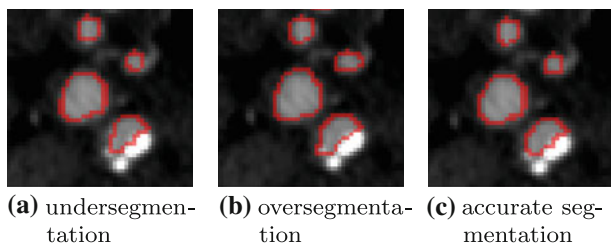


Fig. 8 Illustration of the intensity model parameters on a carotid bifurcation axial slice: **a** the values $k_{\text{near}} = 1.5$, $k_{\text{far}} = 4$ yield suboptimal segmentation that excludes parts of the lumen; **b** the values $k_{\text{near}} = 3.5$, $k_{\text{far}} = 6$ yield oversegmentation that includes parts of the bifurcation stenosis; **c** the values $k_{\text{near}} = 2.5$, $k_{\text{far}} = 5$ yield accurate segmentation that includes the entire lumen while excluding the stenosis

results, we set parameter values to $k_{\text{near}} = 2.5$ and $k_{\text{far}} = 5$. In addition, we set $\sigma_i = \sigma_{\text{vs}}$ for all classes.

The parameters for Frangi's vesselness measure were set to $\alpha = 0.5$, $\beta = 0.5$, $\gamma = 7$, as recommended in [19]. Five equally spaced scales in the 0.5–5.0 mm interval were used to capture the vascular system, which contains a wide range of vessel diameters. The value of α in Eq. 12) was set to $\alpha = 0.25$.

Parameters for the semi-automatic segmentation tool were optimized using 15 training datasets provided by the CLS2009 database [42], and set as follows. For the shortest path computation (Eq. 17), $a = 1$, $b = 1$. The parameter c was used to scale between radian units in the third term and intensity differences, measured in Hounsfield units, with a range of $[-1500, 1500]$. Its values were set to $c = 10,000\pi$. The Euclidean distance was the actual distance in millimeters multiplied by 10,000. The distance factor was set to $k = 2$. The optimization performed using exhaustive search over the parameters ranges with the Dice similarity measure as the optimized function. Note that these 15 training datasets were excluded from the overall evaluation of the method both in [42, 43] and in this paper.

Carotid bifurcation lumen segmentation

We evaluated the performance of both the automatic (“Carotid arteries segmentation”) and semi-automatic methods (“Interactive semi-automatic graph-based vessels connection and cleaning”) with the CLS2009 [42] evaluation framework. The evaluation framework consists of 56 CTA images of the carotid arteries acquired in three medical centers: (1) the Erasmus MC University Medical Center, Rotterdam, The Netherlands (36 datasets); (2) the Hospital Louis Pradel, Bron, France (10 datasets); and (3) the Hadassah-Hebrew University Medical Center, Jerusalem, Israel (10 datasets). For a detailed description of dataset acquisition protocols, contrast agent injection, ground truth generation, and evaluation protocol, see [42].

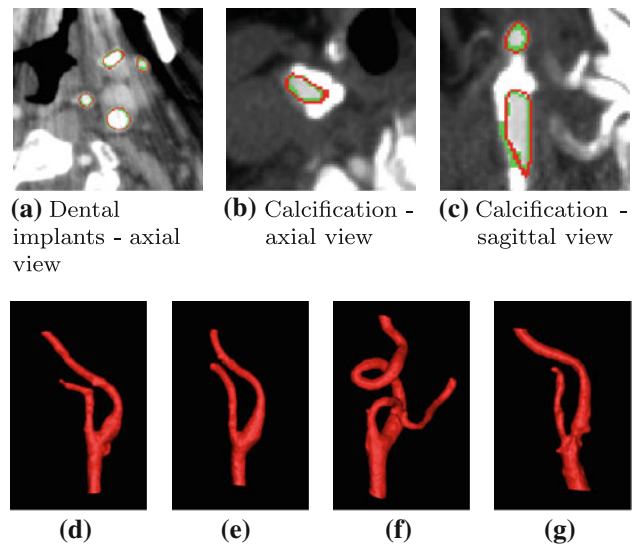


Fig. 9 Final segmentation results: **a–c** 2D views of segmentation results on representative datasets. The resulting segmentation contour (red) is overlaid on the ground truth contour (green); **d–g** spatial visualization of four surface vessel meshes constructed from the automatic segmentation of the carotid bifurcations in the CTA scans

The Hadassah datasets included all the vasculature of interest; the Erasmus and Louis Pradel datasets did not include the aortic arch. The ROI for all datasets includes the CCA, starting at least 20 mm caudal of the carotid bifurcation; the ICA, up to at least 40 mm superior to the carotid bifurcation; and the ECA, up to between 10 and 20 mm superior to the carotid bifurcation. The ground truth for all datasets was generated by averaging the manual segmentations of three expert radiologists. The secondary vasculature of the CCA, ICA, and ECA was not included in the ground truth definition.

The automatic method was evaluated on the 10 Hadassah datasets as the test set; the other datasets were excluded, as they do not include the aortic arch, which is required to construct the IPDF prior. The semi-automatic tool was evaluated on all 56 CTA scans following the workshop methodology. For each scan, three seed points were provided by the workshop organizers as input to the algorithm. From the 56 datasets, 15 were used for training only and the remaining 41 were used for both off-site and on-site evaluations during the workshop [42].

Segmentation accuracy was evaluated by comparing the results to ground truth segmentations generated from three manual annotations with four metrics: (1) mean symmetric absolute surface distance (MSSD); (2) Hausdorff distance (HD); and (3) Dice similarity measure. All of the evaluation measures were performed using the software provided by the CLS2009 workshop organizers [42].

Figure 9 shows the segmentation results of three representative carotid bifurcation cases. Table 1a summarizes

Table 1 Comparison metrics for the first two studies: (a) results for the CLS2009 database and (b) results for the entire carotid system segmentation

	Number of test cases	MSSD (mm)		HD (mm)		Dice (%)		Time (s)			
		Mean	SD	Mean	SD	Mean	SD	Mean	SD	Mean	SD
(a)											
Automatic	10	0.24	0.07	1.55	1.03	90.64	2.5	452	218		
Semi-automatic	41	0.75	0.45	9.2	3.26	82.92	3.42	122	41		
	Number of cases	MSSD (mm)		HD (mm)		Dice (%)		Time (s)		User time (s)	
		Mean	SD	Mean	SD	Mean	SD	Mean	SD	Mean	SD
(b)											
Hadassah	10	0.54	0.16	15.82	4.94	83.67	4.42	470	212	66	12
Rochester	5	0.37	0.04	7.89	2.01	86.16	1.06	154	12	64	17

The first column indicates the method or the origin of the datasets; the second column is the number of datasets; the third column is the mean symmetric surface distance (MSSD) in mm; the fourth column is the Hausdorff distance (HD) in mm; The fifth column is the Dice similarity measure in %; The sixth column is the processing time; The seventh column [(b) only] is the user interaction time required for post-processing

the results of both the automatic and the semi-automatic method. For the automatic method, the mean Dice similarity measure was 90.64% (SD = 2.5%). The MSSD was 0.24 mm (SD = 0.07 mm). The vessel diameter range for the carotid bifurcation region for these datasets was 4–8 mm. For these datasets, the MSSD was 3–6% from the vessel diameter.

For the semi-automatic vessel completion method, the mean Dice similarity measure was 82.92% (SD = 3.42%). The MSSD was 0.75 mm (SD = 0.45 mm), that is, 5–10% from the vessel diameter. The mean computation time for each bifurcation was 122 s (SD = 41 s) using a standard 3 GHz PC with 4 GB of memory. The semi-automatic method ranked 4th among all CLS2009 workshop methods that successfully segmented all 56 datasets, 5th when methods that failed to segment the entire 56 datasets were included, and 3rd for all measures, with the exception of the average HD [42]. We refer the reader to the CLS2009 workshop website (<http://cls2009.bigr.nl/>) for further analysis and comparison with other groups results.

Entire carotid vasculature segmentation

In the second study, we evaluated our segmentation methodology, consisting of automatic segmentation followed by interactive connection and cleaning of the entire carotid vasculature, on 15 CTA scans—10 from the Hadassah-Hebrew University Medical Center, Jerusalem, Israel, and 5 from the Mayo Clinic, Rochester, MN, USA. These datasets were obtained retrospectively and separately, and were not part of the CLS2009 database. In contrast to previously published works [9, 14, 26, 42], our segmentation evaluation included

the entire carotid vasculature, consisting of the aortic arch, the subclavians, and the left and right CCA, ICA, ECA with their secondary vessels. For acquisition of the Hadassah datasets, 10 patients were administered 100 cc of noniodinated contrast material with a rapid injection aid at 3–4 cc s⁻¹. The CTA scans, acquired on a Sensation 16 Siemens Medical Solutions scanner (Forchheim, Germany), have in-plane pixel size 0.5 × 0.5 mm², matrix size 512 × 512, 0.55 mm slice thickness, and 750 slices. For acquisition of the Mayo Clinic datasets, five patients were administered 125 cc of noniodinated contrast material with a rapid injection aid at 5 cc s⁻¹. The CTA scans, acquired on a General Electric Scanner (GE, Milwaukee, USA), have in-plane pixel size 0.35 × 0.35 mm², matrix size 512 × 512, 1.25 mm slice thickness, and 120 slices. Studies from both centers included varying degrees of stenosis and dental implant-related streaking image artifacts. Reference standard segmentation of the arteries were obtained manually by a 3D segmentation expert using the existing ANGIO MentorTM simulation platform [4] and validated by an expert radiologist. For the Rochester datasets, the vertebral arteries were also segmented and used in the evaluation. Both volumetric- and surface-based measures were computed as described in “Carotid bifurcation lumen segmentation.”

Figure 7 shows the segmentation results of three representative cases after automatic segmentation and semi-automatic refinement. Video clips of the 3D models are available in: <http://www.cs.huji.ac.il/~freiman/vessels-cut>.

Table 1b summarizes the results. Our method successfully segmented all datasets and identified all vessels and bifurcations without any failure. The mean Dice similarity measure is 84.5% (SD = 3.3%) and MSSD is 0.48 mm (SD = 0.12 mm). The overall accuracy represents improve-

ment upon our previously published conference paper results [50], in which a different, less effective edge weighting function was used.

The relatively large HD stems from the ground truth aortic arch and subclavian segmentations (Fig. 10). In most cases, the aortic arch and subclavian lumen were conservatively segmented (Fig. 10a, b), yielding a relatively large discrepancy in the surface distance. In addition, aortic arch calcifications were considered as part of the lumen in the manual segmentation, but were not included by our method because of their high intensity values (Fig. 10c).

Figure 11 shows the MSSD box plots of the different vessels diameters in the carotid system for the 15 cases as identified by an expert radiologist. Vessel diameter ranges from 4–8 mm in the region of the carotid bifurcation in the datasets of our study. Segmentation is very accurate on the common carotid and its bifurcation (MSSD is 2.5–5% of the vessel diameter), which are the most important regions for both diagnostic and simulation purposes.

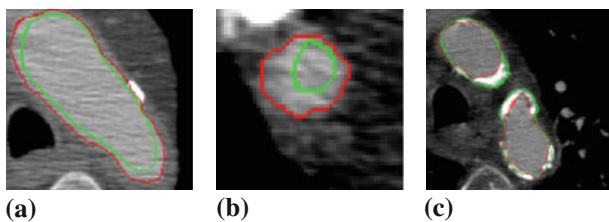


Fig. 10 Illustration of three segmentation discrepancies: the segmentation contour (red) and the ground truth contour (green) are overlaid on the original CTA slice. **a** Aortic arch lumen, **b** subclavian artery lumen **c** aortic arch calcification

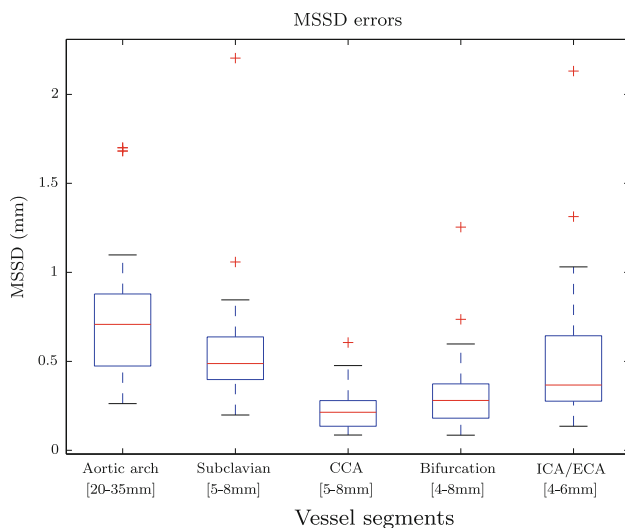


Fig. 11 Box-plot segmentation results of various vessel segments and diameters (the vessel diameter ranges are shown in parenthesis). The red crosses indicate errors that were identified as outliers in the error distribution

Automatic segmentation mean computation time on a standard 3 GHz PC with 4GB of memory was 470 s (SD = 212 s) for the Hadassah scans (high resolution) and 154 s (SD = 12 s) for Rochester scans (lower resolution). The high-resolution images were automatically subdivided into several rectangular blocks to reduce the memory requirements of the graph min-cut algorithm in order to fit the limited memory that was available in the machines participated in this study. The results of the individual runs are then combined into large volume to obtain the entire vasculature system. Semi-automatic refinement required about 10 seed points, usually to connect the carotid arteries and the aortic arch to the subclavians, which have strong artifacts due to the intensity degradation near the shoulders and the high concentration of contrast material close to the injection point. Seed points can be selected on the 3D models directly, or on 2D axial input slices. The overall user time for entire model generation was about ~1 min per dataset.

Patient-specific simulation

In the third study, we performed a preliminary evaluation of the resulting segmentation models for patient-specific carotid interventional radiology simulations. For this purpose, we used a Sionix ANGIO Mentor™ [4] station, an integrated software and hardware endovascular simulation platform (Fig. 12a). The ANGIO Mentor™ simulates interventional vascular procedures based on diagnostic CTA and a vasculature simulation model. It supports realistic haptic catheter insertion and manipulation feedback (Fig. 12b) and creates continuous fluoroscopic X-ray imaging, fluoroscopic C-arm positioning, and simulated contrast agent injection (Fig. 12c).

Simulation models for four Hadassah CTA datasets (“Entire carotid vasculature segmentation”) were generated from segmented CTA images using VMTK software library Marching-cubes automatic meshing and centerline generation modules [51]. Generating the simulation model from the segmentation required a mean computation time of 120 s on a standard PC and 30 s of user time for initialization. Generated meshes were consisted of 150,000 points and 300,000 triangles. Simulation models were then directly transferred to the Sionix ANGIO Mentor™ simulator platform. We then performed common interventional radiology procedures, such as catheter insertion and manipulation, balloon positioning and dilation, and stent placement on the patient-specific models. Fig. 12c–e shows sample snapshots of the simulation with patient-specific models. A video clip showing the simulation with our 3D models is available in <http://www.cs.huji.ac.il/~freiman/vessels-cut>.

Simulations ran flawlessly and successfully in real time for over an hour. Users reported great realism and an excellent overall experience, which was significantly better than

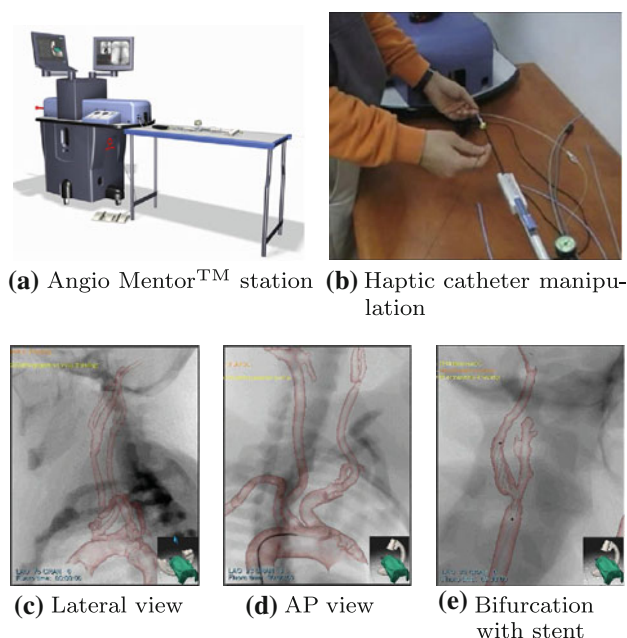


Fig. 12 Patient-specific simulation experiment: **a** the ANGIO Mentor™ simulation station; **b** haptic catheter manipulation; **c** simulated lateral angiogram; **d** simulated anterior–posterior angiogram; **e** detailed view of a bifurcation with stent

similar experiences with the previous manually generated models. While this simulation experiment is qualitative and preliminary, it constitutes a proof-of-concept of practical patient-specific carotid interventional radiology simulations from clinical CTA scans.

Conclusion

We have presented a semi-automatic graph-based method for patient-specific modeling of the aorta and the carotid, vertebral, and subclavian arteries for patient-specific simulations from CTA scans. The method automatically generates a segmentation of the aorta and the entire carotid vasculature, which is then refined with an easy-to-use interactive tool to produce an accurate segmentation from which a simulation model is created. The patient-specific segmentation and simulation model generation from clinical CTA scans takes less than 10 mins of computation time on a standard PC and only about 1 min of end-user interaction. This constitutes a proof-of-concept of practical patient-specific carotid interventional radiology simulations from CTA in a clinical environment. The novelties of our method include (1) coupling between an automatically computed vessel intensity model and local vesselness shape prior for object modeling and adaptive edge weighting; (2) a spatially constrained graph min-cut formulation for automatic vessel segmentation; (3) a semi-automatic graph-based segmentation method for carotid endovascular

patient-specific modeling in a clinical environment; and (4) generation of accurate and robust models for patient-specific simulation. Our extensive, multicenter, multiobserver evaluation results using 71 clinical CTA scans show that the proposed method is accurate, robust, and easy to use, and can be integrated into existing simulators for preoperative patient-specific simulations. The proposed method provides the user with high-quality automatic segmentation of most of the carotid vasculature system with the option to interactively correct segmentation flaws with a few mouse clicks.

We are currently testing and extending our segmentation method to other vascular structures and procedures, such as the liver vasculature and abdominal and thoracic aortic aneurysms. We are also exploring other clinical diagnostic and intraoperative uses of the 3D vascular models, including their possible use for intraoperative navigation support. An extensive evaluation of the patient-specific endovascular simulation is also planned.

Acknowledgments This research is supported in part by MAGNETON grant 38652 from the Israeli Ministry of Trade and Industry. Moti Freiman was also supported in part by the Hebrew University Hoffman Leadership and the Responsibility Fellowship Program. We are grateful to Phillip Berman, Department of Radiology, Hadassah-Hebrew University Medical Center, for his assistance with the Hadassah datasets. The method described in this paper is used for research only and is not part of the commercial Symbionix Ltd. ANGIO Mentor simulator.

Conflict of interest None.

References

- van Bockel JH, Bergqvist D, Cairois M, Liapis CD, Benedetti-Valentini F, Pandey V, Wolfe J, Section E, Vascular Surgery of the European Union of Medical Specialists B (2008) Education in vascular surgery: critical issues around the globe-training and qualification in vascular surgery in europe. *J Vasc Surg* 48:69S–75S; discussion 75S
- Neequaye SK, Aggarwal R, Herzele IV, Darzi A, Cheshire NJ (2007) Endovascular skills training and assessment. *J Vasc Surg* 46:1055–1064
- Verzini F, Rango PD, Parlani G, Panuccio G, Cao P (2008) Carotid artery stenting: technical issues and role of operators' experience. *Perspect Vasc Surg Endovasc Ther* 20:247–257
- Symbionix Ltd. Israel (2008) http://www.symbionix.com/angio_mentor.html
- Stern J, Zeltser I, Pearle M (2007) Percutaneous renal access simulators. *J Endourol* 21:270–273
- Tedesco MM, Pak JJ, Harris EJ, Krummel TM, Dalman RL, Lee JT (2008) Simulation-based endovascular skills assessment: the future of credentialing? *J Vasc Surg* 47:1008–1001 (discussion 1014)
- Berger P, Willems MCM, Vliet JAVD, Kool LJS, Bergqvist D, Blankensteijn JD (2010) Validation of the simulator for testing and rating endovascular skills (stress)-machine in a setting of competence testing. *J Cardiovasc Surg (Torino)* 51:253–256
- Willaert W, Aggarwal R, Nestel D, Gaines P, Vermassen F, Darzi A, Cheshire N (2010) Patient-specific simulation for endovascular procedures: qualitative evaluation of the development process. *Int J Med Robot Comput Assist Surg* 6:202–210

9. Wu X, Luboz V, Krissian K, Cotin S, Dawson S (2011) Segmentation and reconstruction of vascular structures for 3D real-time simulation. *Med Image Anal* 15:22–34
10. Roguin A, Beyar R (2010) Real case virtual reality training prior to carotid artery stenting. *Catheter Cardiovasc Interv* 75:279–282
11. Willaert W, Aggarwal R, Bicknell C, Hamady M, Darzi A, Vermassen F, Cheshire N, (EVEResT), E. V. R. E. R. T. (2010) Patient-specific simulation in carotid artery stenting. *J Vasc Surg* 52:1700–1705
12. Willaert WI, Aggarwal R, Van Herzele I, O'Donoghue K, Gaines PA, Darzi AW, Vermassen FE, Cheshire NJ, On behalf of European Virtual Reality Endovascular Research Team EVEResT (2011) Patient-specific endovascular simulation influences interventionists performing carotid artery stenting procedures. *Eur J Vasc Endovasc Surg* 41:492–500
13. Auricchio F, Conti M, Beule MD, Santis GD, Verhegghe B (2011) Carotid artery stenting simulation: from patient-specific images to finite element analysis. *Med Eng Phys* 33:281–289
14. Manniesing R, Viergever M, Niessen W (2007) Vessel axis tracking using topology constrained surface evolution. *IEEE Trans Med Imaging* 26:309–316
15. Johnson MH, Thorisson HM, DiLuna ML (2009) Vascular anatomy: the head, neck, and skull base. *Neurosurg Clin N Am* 20:239–258
16. Kirbas C, Quek F (2004) A review of vessel extraction techniques and algorithms. *ACM Comput Surv* 36:81–121
17. Lesage D, Angelini E, Bloch I, Funka-Lea G (2009) A review of 3D vessel lumen segmentation techniques: models, features and extraction schemes. *Med Image Anal* 13:819–845
18. Kim D, Park J (2005) Connectivity-based local adaptive thresholding for carotid artery segmentation using MRA images. *Image Vis Comput* 23:1277–1287
19. Frangi A, Niessen W, Vincken K, Viergever M (1998) Multiscale vessel enhancement filtering. In: Proceedings of the 1st international conference on medical image computing and computer assisted interventions, MICCAI'98, vol 1496 of LNCS, pp 130–137
20. Niessen W, van Bommel C, Frangi A, Siers M, Wink O (2002) Model-based segmentation of cardiac and vascular images. In: IEEE international symposium on biomedical imaging, ISBI'02, pp 22–25
21. Lorigo L, Faugeras O, Grimson W, Keriven R, Kikinis R, Nabavi A, Westin C (2001) CURVES: curve evolution for vessel segmentation. *Med Image Anal* 5:195–206
22. Nain D, Yezzi A, Turk G (2004) Vessel segmentation using a shape driven flow. In: Proceedings of the 7th international conference on medical image computing and computer assisted interventions, MICCAI'04, vol 3216 of LNCS, pp 51–59
23. Scherl H, Hornegger J, Prümmer M, Lell M (2007) Semi-automatic level-set based segmentation and stenosis quantification of the internal carotid artery in 3D CTA data sets. *Med Image Anal* 11:21–34
24. Tang H et al (2010) A semi-automatic method for segmentation of the carotid bifurcation and bifurcation angle quantification on black blood MRA. *Med Image Comput Assist Interv* 13:97–104
25. Manniesing R, Schaap M, Rozie S, Hameeteman R, Vukadinovic D, van der Lugt A, Niessen W (2010) Robust CTA lumen segmentation of the atherosclerotic carotid artery bifurcation in a large patient population. *Med Image Anal* 14:759–769
26. Lekadir K, Merrifield R, Guang-Zhong Y (2007) Outlier detection and handling for robust 3-D active shape models search. *IEEE Trans Med Imaging* 26:212–222
27. Schaap M, Manniesing R, Smal T, van Walsum I, van der Lugt A, Niessen W (2007) Bayesian tracking of tubular structures and its application to carotid arteries in CTA. In: Proceedings of the 10th international conference on medical image computing and computer assisted interventions, MICCAI'07, vol 4792 of LNCS, pp 562–570
28. Friman O, Hindennach M, Kuhnel C, Peitgen H-O (2010) Multiple hypothesis template tracking of small 3D vessel structures. *Med Image Anal* 14:160–171
29. Tek H, Gulsun M (2008) Robust vessel tree modeling. In: Proceedings of the 11th international conference on medical image computing and computer assisted interventions, MICCAI'08, vol 5241 of LNCS, pp 602–611
30. Suryanarayanan S, Mullick R, Mallya Y, Kamath V, Nagaraj N (2004) Automatic partitioning of head CTA for enabling segmentation. In: Fitzpatrick J, Sonka M (eds) SPIE medical imaging, vol 5370, SPIE, San-Diego, pp 410–419. <http://dx.doi.org/10.1117/12.533933>
31. Cuisenaire O, Virmani S, Olszewski ME, Ardon R (2008) Fully automated segmentation of carotid and vertebral arteries from contrast enhanced CTA. *Proc SPIE* 6914:69143R. <http://dx.doi.org/10.1117/12.770481>
32. Cuisenaire O (2009) Fully automated segmentation of carotid and vertebral arteries from CTA. *Midas J*. <http://hdl.handle.net/10380/3100>
33. Boykov Y, Funka-Lea G (2006) Graph cuts and efficient n-d image segmentation. *Int J Comput Vision* 70:109–131
34. Kang L, Xiaodong W, Chen D, Sonka M (2006) Optimal surface segmentation in volumetric images—a graph-theoretic approach. *IEEE Trans Pattern Anal Mach Intell* 28:119–134
35. Kolmogorov V, Boykov Y (2005) What metrics can be approximated by geo-cuts, or global optimization of length/area and flux. In: Proceedings of the tenth IEEE international conference on computer vision, ICCV 2005, vol 1, pp 564–571
36. Sinop AK, Grady L (2007) A seeded image segmentation framework unifying graph cuts and random walker which yields a new algorithm. In: Proceedings of the IEEE 11th international conference on computer vision, ICCV 2007, pp 1–8
37. Vicente S, Kolmogorov V, Rother C (2008) Graph cut based image segmentation with connectivity priors. In: Proceedings of the international conference on computer vision and pattern recognition, CVPR 2008, pp 1–8
38. Slabaugh G, Unal G (2005) Graph cuts segmentation using an elliptical shape prior. In: Proceedings of the 2005 IEEE international conference on image processing, ICIP'05, vol 2, pp 1222–5
39. Bauer C, Pock T, Sorantin E, Bischof H, Beichel R (2010) Segmentation of interwoven 3D tubular tree structures utilizing shape priors and graph cuts. *Med Image Anal* 14:172–184
40. Schaap M, Neeffjes L, Metz C, Giessen A, Weustink A, Mollet N, Wentzel J, Walsum T, Niessen W (2009) Coronary lumen segmentation using graph cuts and robust kernel regression. In: Proceedings of the 21st international conference on information processing in medical imaging, IPMI'09, vol 5636 of LNCS, pp 528–539
41. Homann H, Vesom G, Noble J (2008) Vasculature segmentation of CT liver images using graph cuts and graph-based analysis. In: IEEE international symposium on biomedical imaging, ISBI'08, pp 53–56
42. Hameeteman K, Zuluaga MA, Freiman M, Joskowicz L, Cuisenaire O, Flórez Valencia L, Gülsün MA, Krissian K, Mille J, Wong WCK, Orkisz M, Tek H, Hernández Hoyos M, Benmansour F, Chung ACS, Rozie S, van Gils M, van den Borne L, Sosna J, Berman P, Cohen N, Douek PC, Sánchez I, Aissat M, Schaap M, Metz CT, Krestin GP, van der Lugt A, Niessen WJ, van Walsum T (2011) Evaluation framework for carotid bifurcation lumen segmentation and stenosis grading. *Med Image Anal* 15(4):477–488. doi:10.1016/j.media.2011.02.004. <http://www.sciencedirect.com/science/article/pii/S1361841511000260>
43. Freiman M, Frank J, Weizman L, Nammer E, Shilon O, Joskowicz L, Sosna J (2009) Nearly automatic vessels

- segmentation using graph-based energy minimization. Midas J. <http://hdl.handle.net/10380/3090>
44. Roerdink J, Meijster A (2000) The watershed transform: definitions, algorithms and parallelization strategies. *Fundam Inf* 41:187–228
 45. Gonzalez RC, Woods RE (2006) *Digital image processing*, 3rd edn. Prentice-Hall, Inc, Englewood Cliffs, NJ
 46. Freiman M, Eliassaf O, Taieb Y, Joskowicz L, Sosna J (2008) A bayesian approach for liver analysis: algorithm and validation study. In: *Proceedings of the 11th international conference on medical image computing and computer aided interventions, MIC-CAI'08*, vol 5241 of LNCS, pp 85–92
 47. Kolmogorov V, Zabih R (2004) What energy functions can be minimized via graph cuts? *IEEE Trans Pattern Anal Mach Intell* 26:147–159
 48. Dijkstra EW (1959) A note on two problems in connexion with graphs. *Numerische Mathematik* 1:269–271
 49. <http://www.itk.org>
 50. Freiman M, Broide N, Natanzon M, Weizman L, Nammer E, Shilon O, Frank J, Joskowicz L, Sosna J (2009) Vessels-cut: a graph based approach to patient-specific carotid arteries modeling. In: *Proceedings of the 2nd 3D physiological human workshop, 3DPH'09*, vol 5903 of LNCS, pp 1–12
 51. Antiga L, Steinman D (2004) Robust and objective decomposition and mapping of bifurcating vessels. *IEEE Trans Med Imaging* 23:704–713. <http://www.vmtk.org>